



Cite this: DOI: 10.1039/c8nr07823h

## Charge transfer from internal electrostatic fields is superior to surface defects for 2,4-dichlorophenol degradation in $K_{3-x}Na_xB_6O_{10}Br$ photocatalysts†

Xiaoyun Fan, \*<sup>a</sup> Yang Zhang<sup>a</sup> and Kangdi Zhong<sup>b</sup>

Both surface oxygen vacancies and bulk motivation in a semiconductor play very important roles in the photocatalytic process. To distinguish between the roles of bulk motivation and the surface state in a photocatalytic process, two different phases of K–B–O–B (KBB) photocatalysts with built-in electric field or surface oxygen vacancies were fabricated *via* the addition of different amounts of Na<sup>+</sup> substitute. The crystal structure, band structure, reactive species and photocatalytic performance of two types of photocatalysts were systematically investigated. For the six studied photocatalysts,  $K_3B_6O_{10}Br$  (KBB1),  $K_{2.87}Na_{0.13}B_6O_{10}Br$  (KBB2), and  $K_{2.33}Na_{0.67}B_6O_{10}Br$  (KBB3) with less Na<sup>+</sup> content behaved as polar materials, while  $K_{1.7}Na_{1.3}B_6O_{10}Br$  (KBB4),  $K_{0.80}Na_{2.20}B_6O_{10}Br$  (KBB5), and  $Na_3B_6O_{10}Br$  (KBB6) with more Na<sup>+</sup> content behaved as nonpolar materials. Among them, KBB3 exhibited the best photocatalytic activity, which was about 1.15, 1.07, 1.4, 1.25, and 1.18 times that of the KBB1, KBB2, KBB4, KBB5 and KBB6 samples, respectively. During the degradation process of 2,4-dichlorophenol (2,4-DCP), the dominant reactive oxidation species was mainly  $\cdot O_2^-$ , while the  $\cdot OH$  and  $h^+$  played secondary roles. The oxygen vacancy concentration increased as the Na atoms increased for the polar materials, except for KBB1; the oxygen vacancy and the built-in electric field had a synergistic effect on the degradation process to nonpolar materials, with the main active species coming only from the high concentration of oxygen vacancies. Furthermore, the activity of KBB1 with only the built-in electric field was superior to that of KBB6 with surface oxygen vacancies, which further confirmed that for charge separation, the driving force from the bulk could provide more motivation than surface defects during the 2,4-DCP degradation process.

Received 26th September 2018,  
Accepted 18th October 2018

DOI: 10.1039/c8nr07823h

rsc.li/nanoscale

## Introduction

Photocatalysis has become increasingly important for solving the conflict of environmental issues and worldwide energy in recent years. In the photocatalytic system, the photoinduced electron–hole pairs separate and are transferred to the surface of a semiconductor to take part in the reaction. There are several parameters that influence the charge transfer efficiency, including crystal structure, band-gap energy, phase structure, specific surface area, crystallite size, and surface properties of the semiconductor, *etc.*<sup>1–3</sup> On this basis, many approaches have been developed to promote the solar energy conversion efficiency, such as the development of active facet

tailoring,<sup>4–6</sup> conduction in the heterojunction structure,<sup>7,8</sup> modification of surface defects, and so forth.<sup>9–11</sup>

Surface oxygen vacancies are surface defects of the photocatalyst, which have a significant influence on the electronic structure of the photocatalyst and are beneficial for light absorption.<sup>12</sup> The importance of oxygen vacancies is that after the formation of vacancies, the reaction sites are more abundant or the migration of oxygen vacancies becomes possible. Photo-induced electrons in the conduction band (CB) are preferentially transferred to oxygen vacancies, which can be the centre for the trapping of photo-induced electrons in the photo-induced reaction, making the separation of photo-induced charges easier.<sup>13–15</sup> On the other hand, the materials with polar structure usually have ferroelectric characteristics producing spontaneous polarization properties, which can be considered as a strong motivation for the separation of photo-induced charges.<sup>16,17</sup> When there is a built-in electric field in the bulk oxide, holes left on the surface will shift along the electric field direction, while excited electrons will migrate to the surface in the opposite direction of the electric field.<sup>18,19</sup>

<sup>a</sup>School of Environment and Guangdong Key Laboratory of Environmental Pollution and Health, Jinan University, Guangzhou 510632, China. E-mail: xyfan@jnu.edu.cn

<sup>b</sup>Department of Physics, Changji University, Changji, 830011, China

†Electronic supplementary information (ESI) available: Experimental details, material characterization methods, performance evaluation method and some supplementary figures. See DOI: 10.1039/c8nr07823h

Under these circumstances, the photogenerated charges can be easily separated for redox reactions at different surface sites. Recently, our group successfully synthesized a series of materials with polar structures that showed excellent dechlorination properties under photoirradiation.<sup>20</sup> These works undoubtedly revealed that the materials with bulk motivation could act as a strong driving force for the charge transfer during the photocatalytic process. Based on these two states, the question arises as to which part would be more important for promoting the photocatalytic performance in a material, surface defects or the bulk motivation? However, very little attention has been paid to this issue to date. To this end, it was our intention to construct a material with oxygen defects or a built-in electric field to reveal the relationship between two correlated influencing factors in boron–oxygen based photocatalysts.

In order to distinguish the roles of bulk motivation and surface state in a photocatalytic process, the fabrication of an appropriate reaction system in which these two roles are separated in different active sites is of great necessity. Usually, the substitution of a similar coordination environment or ionic radius takes place easily in the synthesis process, with the accompanying formation of oxygen vacancies in order to maintain the charge equilibrium. When the content of the substituted atoms exceeds a certain amount, a phase change will take place due to the rich energy levels and special electronic transition properties<sup>21</sup> and, therefore, the electric field can be controllable.<sup>22</sup> The change in lattice constants will lead to the photoexcited charge delocalization, which might affect the possibility of electrons reaching the reaction sites on the surface of the photocatalyst.<sup>23</sup>

In this study, we synthesized a series of K–B–O–B (KBB) materials,  $M_2CO_3\text{-MBr-B}_2O_3$  ( $M = K, Na$ ) alkali borate crystals; by changing the content of the substituted Na atoms, the concentration of the oxygen vacancies and the phase transition can be tuned. Moreover, with the increase in the Na content, the crystal structure will be transformed from a polar  $R3m$  structure, into a nonpolar  $Pnma$  structure. It was also found that substitution of  $K^+$  by  $Na^+$  resulted in different photocatalytic performance properties. From the ESR and KPFM experiment, we confirmed that the materials with internal electric fields showed better activity performance than those with only oxygen vacancies.

## Results and discussion

The powder XRD patterns of KBB1–KBB6 samples are illustrated in Fig. 1a. Compared to  $K^+$  ions,  $Na^+$  ions have a smaller radius and different electronic structure, which results in different bonding effects. The intensities of the peaks at  $2\theta$  values of 27.2 and 28.8 became weak with the increasing substituted content. When most of the  $K^+$  ions were substituted by  $Na^+$  ions in the KBB crystal, different peaks would be seen. As the content of  $Na^+$  exceeded 1.3 (mole ratio), there were obvious changes in the peaks at  $2\theta$  values of 27.8, 28.2, 29.0, and 29.8 in the samples of KBB4–KBB6 (Fig. 1b).

The studied six samples crystallized in a perovskite structure, with KBB1–KBB3 samples having an  $R3m$  phase and KBB4–KBB6 having a monoclinic phase. The similarity of the crystal structure for KBB3 and the classic  $R3m$  perovskite  $CaTiO_3$  compounds have been described in Fig. S1 in the ESI.† The DRS spectra of the KBB series photocatalysts are shown in Fig. 1c. These photocatalysts display UV-visible absorption, with an absorption onset at around 340 nm. The band gaps of the KBB1–KBB3 and KBB4–KBB6 photocatalysts were estimated to be about 3.5 and 3.2 eV, respectively, indicating the decrease in the band gap when substituted with the smaller  $Na^+$  ions, which further confirmed that the conduction band (CB) and valence band (VB) potentials could be tuned by controlling the sodium concentration.

The theoretical band structure of KBB samples was determined to predict the positions of the band by the following eqn (1) and (2):<sup>24</sup>

$$E_{CB} = \chi - E_e - 0.5E_g \quad (1)$$

$$E_{VB} = E_{CB} + E_g \quad (2)$$

where  $\chi$  is the electronegativity of the semiconductor, which is the geometric mean of the electronegativity of the constituent atoms ( $\chi_K = 2.7882$  eV,  $\chi_{Na} = 2.5378$  eV,  $\chi_B = 4.5951$  eV,  $\chi_O = 8.3703$  eV), and  $\chi = (\chi_A^a \times \chi_B^b \times \chi_C^c)^{(a+b+c)^{-1}}$  of semiconductor  $A_aB_bC_c$ ;  $E_g$  is the band gap energy of the semiconductor;  $E_{VB}$  is the valence band (VB) edge potential;  $E_{CB}$  represents the conduction band (CB) edge potential;  $E_e$  represents the energy of free electrons on the hydrogen scale (4.5 eV).<sup>24,25</sup> The values of calculated  $\chi$ ,  $E_{VB}$ ,  $E_{CB}$  and  $E_g$  are listed in Table 1 and Fig. 2. The  $Na^+$  ions definitely influenced the optical properties of the

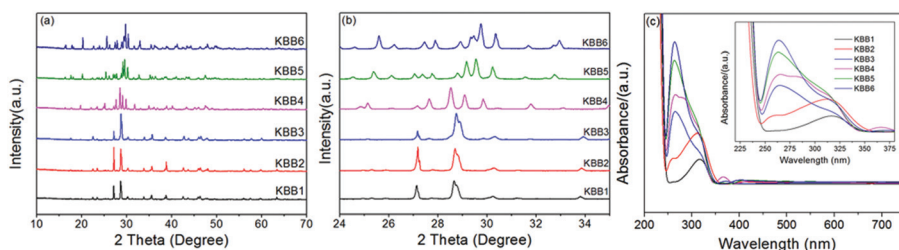
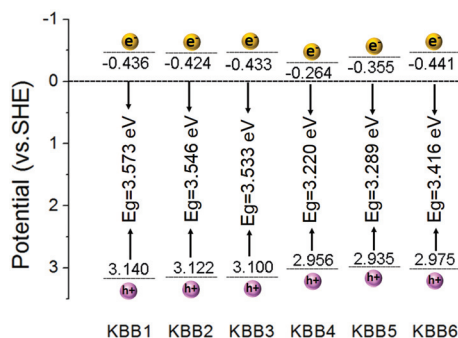
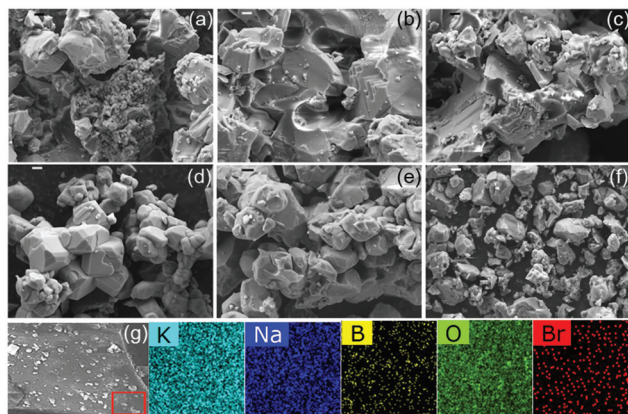


Fig. 1 XRD patterns of the KBB samples (a) and (b). The UV-vis DRS of the KBB1–KBB6 samples (c); the inset displays the magnified peaks.

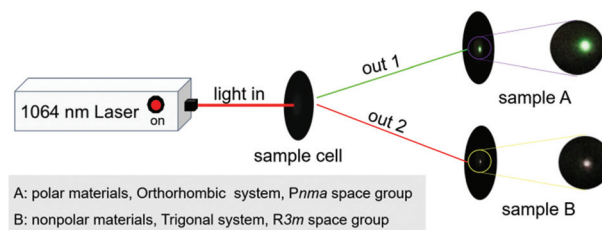
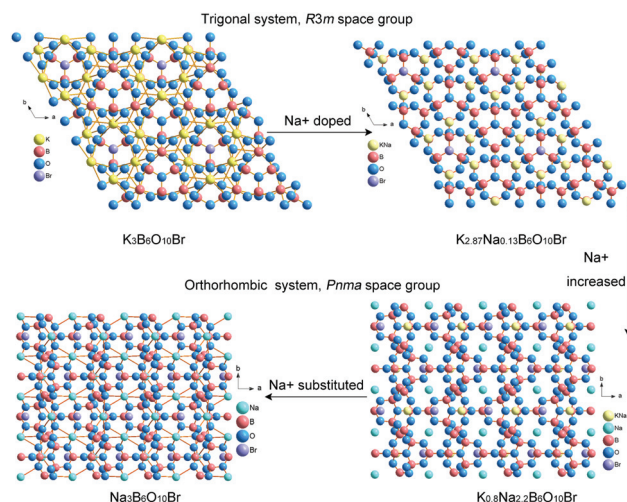
**Table 1** Band structure of the samples

Samples	$X$	$E_g$ (eV)	$E_{CB}$ (eV)	$E_{VB}$ (eV)
KBB1	5.853	3.573	-0.436	3.140
KBB2	5.849	3.546	-0.424	3.122
KBB3	5.834	3.533	-0.433	3.10
KBB4	5.816	3.220	-0.264	2.956
KBB5	5.790	3.289	-0.355	2.935
KBB6	5.767	3.416	-0.441	2.975

**Fig. 2** Band structures of the KBB samples.**Fig. 3** SEM of KBB1 (a), KBB2 (b), KBB3 (c), KBB4 (d), KBB5 (e) and KBB6 (f) samples and EDS mappings of the KBB3 samples (g). Scale bar is 500 nm.

crystal. SEM images of the six samples are depicted in Fig. 3, where we clearly see that all samples had irregular morphologies. The presence of K, Na, B, O, and Br was confirmed by energy dispersive spectroscopy (EDS) analysis.

It has been described that KBB1–KBB3 show similar XRD patterns, while KBB4–KBB6 are alike. Therefore, we deduced that the two series of materials had different phase structures. Usually, the SHG signal can only be produced in a non-centric structure, which is used to determine the ferroelectric properties of a material.<sup>26</sup> Thus, we adopted the SHG approach to distinguish these two different series of materials. The KBB1–KBB3 materials exhibited remarkable double frequency emission at 532 nm, indicated by a green spot in Fig. 4. However,

**Fig. 4** SHG test for materials with different structures upon 1064 nm laser irradiation. Sample A represents non-centric materials, and sample B represents centric materials.**Fig. 5** The increase in Na content induces a phase transition.

such a green spot was not observed for KBB4–KBB6 materials, due to their centrosymmetric structure. The KBB1–KBB3 samples crystallize in a trigonal structure (space group:  $R3m$ ) and behave as polar materials, while KBB4–KBB6 have a centrosymmetric structure (space group:  $Pnma$ ) and perform as nonpolar materials. These differences are closely related to the coordination environments of the Br atoms and the difference in  $[B_6O_{10}]$  unit alignment. In the polar structure, a single Br atom is bound to six metal atoms and the  $[B_6O_{10}]$  groups are aligned in parallel in the Br-metal framework (Fig. S2a and S2b<sup>†</sup>). In the nonpolar structure, the Br atoms are coordinated by two Na atoms, two K atoms, and two K/Na atoms and the  $[B_6O_{10}]$  groups are antiparallel into the Br-metal structure (Fig. S2c and S2d<sup>†</sup>).<sup>27</sup>

We further increased the Na ion content and investigated its effect on the structure of the materials. Fig. 5 shows that substituting with a low content of  $Na^+$  ions did not produce any crystalline phase change. However, due to the different ionic radii of the  $K^+$  and  $Na^+$  cations, the lattice parameters became smaller and smaller as the content of  $Na^+$  increased.<sup>28,29</sup> It was further confirmed that element substitution can change the cell parameters of the crystal when the host ionic radius is much different, which will induce lattice

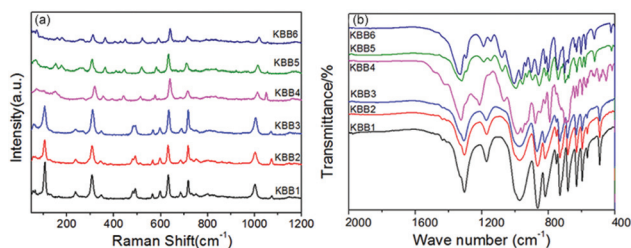


Fig. 6 Raman spectra (a) and FTIR spectra (b) of KBB1–BB6 photocatalysts.

distortion and change the crystallite size. Consequently, the substitution of  $\text{Na}^+$  for the  $\text{K}^+$  sites led to the B–O chain distortion and induced the transformation from  $R3m$  into the  $Pnma$  structure.

By conducting Vis-Raman and IR spectroscopy, we investigated the structural information of KBB1–KBB6 catalysts (Fig. 6a). As expected, due to the difference in the crystal structure, the partial peaks of the KBB1–KBB3 samples were much weaker and broader compared to the KBB4–KBB6 samples. The peak position and the attributions are as follows: the typical bands for KBB1–KBB3 are located at 1312, 1149, 1071, 1001, 809, 750, 716, 685, 630, 597, 566, 491–478, 347, 306, 238, and 105–58  $\text{cm}^{-1}$ . The peak at 1321  $\text{cm}^{-1}$  is attributed to an asymmetric stretching of the  $\text{BO}_3$  bond and the peaks between 1149  $\text{cm}^{-1}$  and 1001  $\text{cm}^{-1}$  are assigned to the asymmetric stretching of the  $\text{BO}_4$  bond. The peaks at 809  $\text{cm}^{-1}$  and around 594  $\text{cm}^{-1}$  are due to symmetric stretching of the terminal  $\text{BO}_3$  and  $\text{BO}_4$  bonds, while the peaks at 750–630 and 238–347  $\text{cm}^{-1}$  are attributed to the bending vibrations of terminal  $\text{BO}_3$  and  $\text{BO}_4$ , respectively. The peaks below 105  $\text{cm}^{-1}$  represent the deformations of B–O–B. After the ratio of the Na atoms exceeds 1.3, more Raman peaks appeared due to the restructuring of the surface B–O species and the phase transition induced by the lattice structure.<sup>28</sup> The main peaks for KBB4–KBB6 were located at 1349, 1169, 1120, 1057, 1015, 823, 800, 716, 709, 630, 590–582, 519, 445, 363, 308, 240–267, and 176–72  $\text{cm}^{-1}$ . Compared to KBB1–KBB3 samples, all the peaks obviously shifted to higher wavenumbers, which shows that the substitution of K for KBB4–KBB6 will result in less disturbance to the structure as compared to Na. In the FTIR spectra, KBB1–KBB3 samples exhibited similar absorption; however, as the Na atom content increased, the intensity became weak and some shifts appeared for KBB4–KBB6 samples. The Raman shifts and FTIR spectra of these composites have been shown in Fig. 6b and Table S1.†

The dechlorination rate result is shown in Fig. 7a, where it can be seen that when the Na atoms are not the predominant components, the photoactivity is promoted as the content of Na atoms increases, and the KBB3 sample has the best photo-degradation performance. When the Na atom content increased to a ratio exceeding 1.3, there was a drastic decrease in the photocatalytic performance for the KBB4 sample. However, after that, the activity of the KBB5 and KBB6 samples

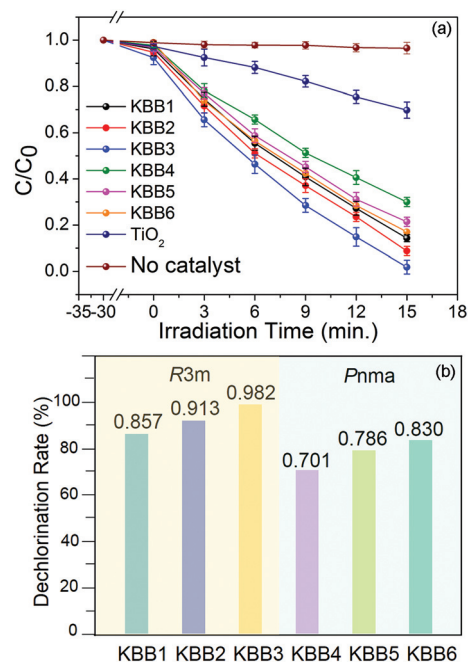
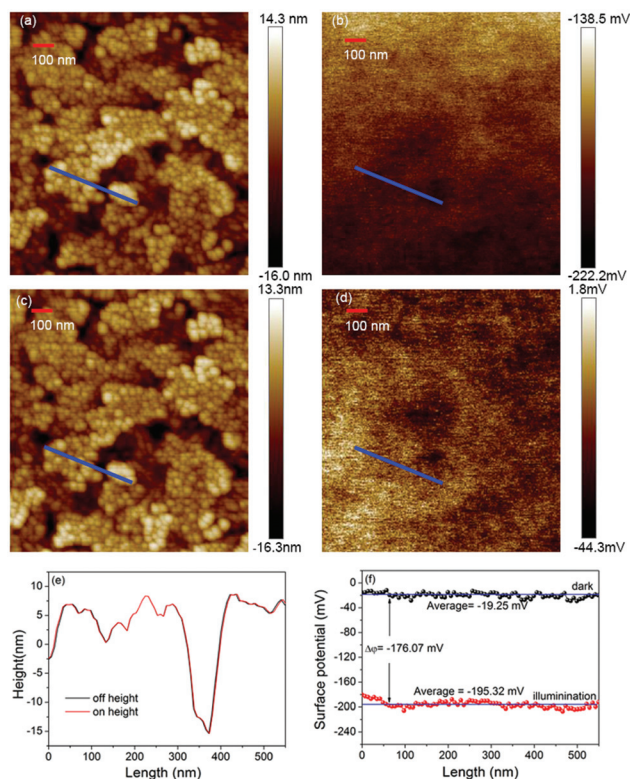


Fig. 7 Photocatalytic degradation of 2,4-DCP under UV-visible light irradiation over different samples (a). A comparative representation of the 2,4-DCP degradation efficiency for two different phase structures (b).

showed a stepwise increase, and the KBB6 sample had the highest activity (Fig. 7b). We can conclude that the overall degradation levels for polar materials are better as compared to the nonpolar materials. Compounds like hydroquinone and hydroxy hydroquinone are the predominant intermediates formed during the photocatalytic degradation of 2,4-DCP, which were identified by the LC-MS method, shown in Fig. S3 and Table S2.† It is known that surface area is a key influencing factor in the photocatalytic process, thus BET measurements were taken for the KBB1–KBB6 series and  $\text{TiO}_2$ . From Fig. S4,† it can be seen that the surface areas of the KBB series of photocatalysts are relatively small; thus, we can deduce that the excellent photo activity performance of such materials might be caused by their intrinsic structure.

The built-in potential is an intrinsic characteristic of the polar materials, which is feasible for promoting light-separation efficiency. In bulk systems, at thermal equilibrium, atomic force microscopy (AFM) and Kelvin probe force microscopy (KPFM) can be used to analyse the surface potential difference between the irradiated and non-irradiated areas.<sup>30</sup> The overall topography and KPFM potential measurements for KBB1 were tested simultaneously *via* one pass. Fig. 8a and b show the morphology and the surface potential for the sample before light irradiation, while Fig. 8c and d show the morphology of the sample after light irradiation. Different colours in the KPFM show different Fermi levels; the light area with high surface potential indicates a shallow Fermi Level, while the dark area with low surface potential represents a deep Fermi level.<sup>31</sup> In Fig. 8e, the morphology image



**Fig. 8** AFM images of KBB1 before (a) and after (c) UV-visible light irradiation and the corresponding surface potential images of KBB3 before (b) and after (d) UV-visible light irradiation. (e) Height differential curve along the blue line from panel (a) and panel (c). (f) Surface potential profile along the blue line in panel b and panel d.

shows no changes, while the SP images change obviously. There is a decrease of about 167 mV on average when under illumination, as shown in Fig. 8f, which is due to the fact that the surface band was downward-bent during the photoexcitation process. The AFM and KPFM analysis for KBB3 are shown in Fig. S5 in the ESI.† It can be clearly seen that the value of the surface potential changes for KBB1 is a bit smaller compared with the KBB3 before and after light illumination, which is consistent with their performance activity.

During the synthesis process, the substituted Na atoms with different atomic and electronic structures undergo distortion to generate oxygen vacancies.<sup>32</sup> This result was confirmed by ESR characterization of the as-synthesized materials, shown in Fig. 9. Except for KBB1, the other 5 samples share a typical signal at approximately  $g = 2.00$ , indicating the presence of the intrinsic oxygen vacancies.<sup>33</sup> It is considered that the broad and strong intensity of the ESR signals usually indicates the existence of a higher concentration of oxygen vacancies. Obviously, from the ESR result, the intensity of the oxygen vacancy shows a significant increase after the phase transition. We can clearly find that the signals of the KBB4–KBB6 samples are remarkably stronger than that of KBB2 and KBB3 samples, which coincides well with the increasing content of the Na atoms. The calcination temperature of KBB4–KBB6 was

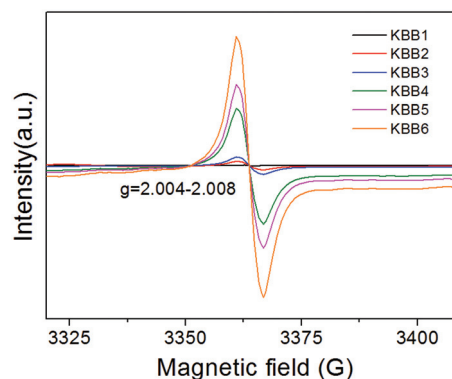


**Fig. 9** ESR spectra of KBB1–KBB6 samples.

higher than that of KBB2 and KBB3, which helped to introduce  $\text{Na}^+$  species into the KBB lattice; the partial substitution of  $\text{K}^+$  species led to the formation of abundant oxygen vacancies. Therefore, we concluded that the oxygen vacancy concentration could be precisely tuned by the substituted content and phase transition.<sup>34–36</sup>

In order to distinguish between the existence of bulk or surface oxygen vacancies in the materials, we adopted thermogravimetric analysis (TGA) to detect the mass change in the air atmosphere.<sup>37,38</sup> Considering that the studied materials were unstable at a high temperature above 720 °C, we analysed the thermal behaviour of the studied materials below this temperature. From TGA results, as shown in Fig. S6,† we can clearly see that the mass loss for the KBB series in the low-temperature range is mainly ascribed to the desorption of physically adsorbed  $\text{H}_2\text{O}$  and other small molecules. After that, for KBB1–KBB3 samples, the mass increase was not obvious and even showed a negligible decrease when the temperature arrived at 720 °C. However, there was a slight mass increase for KBB4–KBB6 samples due to the existence of a large number of oxygen vacancies on the surface, and the unsaturated surface would be compensated for by the oxygen when heated in air. Compared to KBB1–KBB3 samples, the mass increase for KBB4–KBB6 samples was more apparent, indicating a greater concentration of oxygen vacancies and a much easier oxygen compensation for the surface oxygen vacancies.

Furthermore, the investigations have indicated that surface defects play an important role in increasing the surface active sites, which is beneficial to the improvement of photocatalytic activity, while the bulk defects are the capture centres for photogenerated charges.<sup>39</sup> As a recombination centre for electron–hole pairs, the photocatalytic performance of the catalyst is largely inhibited. From Fig. 9, it can be clearly seen that the surface oxygen vacancy increased as the substituted contents increased for the KBB4–KBB6, resulting in an increase in photocatalytic activity (Fig. 7). Thus, we can conclude that the surface oxygen vacancies, rather than bulk oxygen vacancies, were fabricated *via* the addition of different amounts of  $\text{Na}^+$  substituents.

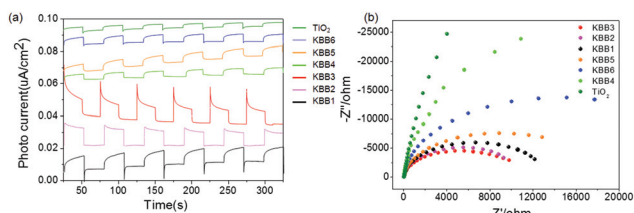


Fig. 10 (a) Photocurrent response and (b) EIS Nyquist plots of KBB1–KBB6 samples under UV-visible light illumination ( $\lambda > 320$  nm).

The photocurrent density was further determined to confirm the above results. As shown in Fig. 10a, KBB1–KBB3 had a much larger photo-current density as compared to KBB4–KBB6. The charge transfer resistance across the electrode interface of polar material was much smaller than that of the nonpolar photocatalyst, indicating that the polar materials had a lower resistance value for electron transfer (Fig. 10b). This phenomenon was further confirmed by the PL spectrum, which involved the competitive formation of electron–hole pairs and their recombination. Fig. S7† shows the PL spectra of KBB1–KBB6 samples and the emission peaks of all samples are similar but the intensities are different. In general, the photocatalyst with a higher photocatalytic activity usually has a lower PL intensity. The intensities of the PL spectra of KBB1–KBB3 are lower, which means that the electron pair recombination is largely suppressed. Among the non-polar materials, KBB4 showed the strongest intensity, indicative of the highest rate of e–h recombination, and the intensity decreased with the increase in Na atoms, suggesting a greater separation efficiency of electrons and holes. The structural parameters, surface area, photocurrent ratio, and degradation rates of KBB samples are summarized in Table 2, which clearly imply that KBB3 has the optimized ratio of Na-substituted samples. Therefore, we performed cycling experiments using the KBB3 sample. From Fig. 11a, it can be seen that the degradation efficiency had a minor decrease but almost maintained the same level as the original after four cycling experiments; also the crystal structures of the photocatalysts showed negli-

Table 2 Structural parameters, surface area, photocurrent ratio and degradation rates of KBB samples

Sample	K, Na mole ratio		SA m g <sup>-1</sup>	I/I <sub>0</sub>	DE
	K	Na			
KBB1	3	0	3.817	0.61	85.7
KBB2	2.87	0.13	2.655	0.78	91.3
KBB3	2.33	0.67	3.127	1.02	98.2
KBB4	1.7	1.3	4.425	0.25	70.1
KBB5	0.8	2.2	0.765	0.39	78.6
KBB6	0	3	3.537	0.45	82.9
P25	—	—	52.325	0.076	30.2

SA = surface area; I/I<sub>0</sub> = photocurrent ratio; De = degradation efficiency.

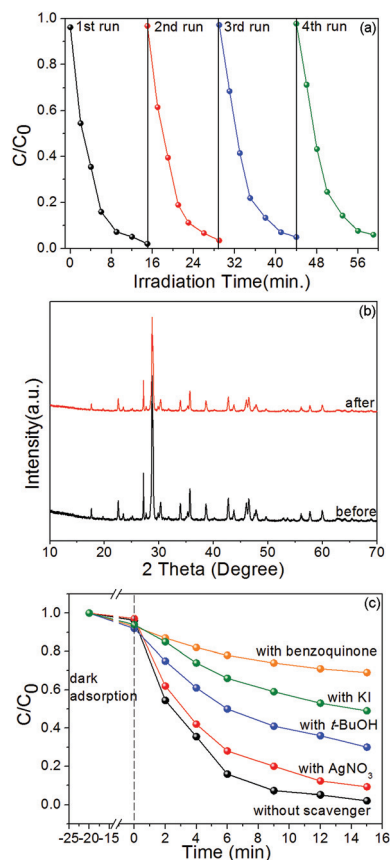
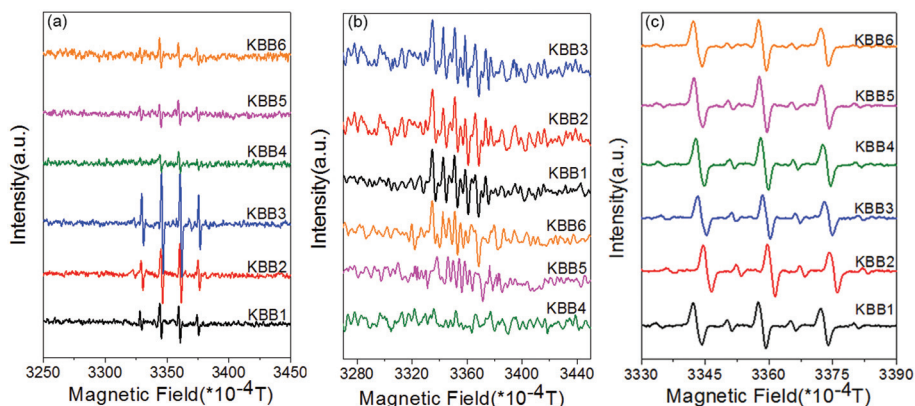


Fig. 11 Four cycle degradations of 2,4-DCP (a); comparison of XRD patterns before and after the four photodegradation experiments (b); degradation curves of 2,4-DCP with different scavengers in the presence of KBB3 under the UV-visible light ( $\lambda > 320$  nm) irradiation (c).

gible changes in the XRD results (Fig. 11b), indicating the stability of the KBB samples.

The photocatalytic 2,4-DCP degradation reaction in aqueous solution took place under an air atmosphere; ROS such as superoxide ( $\cdot\text{O}_2^-$ ), hydroxyl ( $\cdot\text{OH}$ ), and singlet oxygen ( $^1\text{O}_2$ ) play important roles during the photocatalytic process.<sup>40,41</sup> To confirm the occurrence of these species in the present photocatalytic system, ESR spectra of the solution were obtained for  $\cdot\text{OH}$ , and  $^1\text{O}_2$ , respectively. A quartet of signals with relative intensities of 1:2:2:1 from the DMPO- $\cdot\text{OH}$  adducts were detected, denoting that  $\cdot\text{OH}$  was present in the reaction process (Fig. 12a), while a 6-fold ESR peak with characteristics of DMPO- $\cdot\text{O}_2^-$  appeared with the addition of DMPO/DMSO agents (Fig. 12b),<sup>42</sup> demonstrating that the photogenerated electrons in the conduction band of the catalyst could be transformed into  $\cdot\text{O}_2^-$  radicals in the present catalytic system.<sup>43</sup> Three ESR peaks with an intensity ratio of 1:1:1 is consistent with the formation of the TEMP- $^1\text{O}_2$  adduct from the addition of TEMP, suggesting that singlet oxygen is involved in the decomposition,<sup>44</sup> as shown in Fig. 12c. It is obvious that all KBB samples had similar intensity, revealing that  $^1\text{O}_2$  takes part in the photocatalytic reaction but plays the same role in the photocatalytic system. From the



**Fig. 12** Comparison of ESR intensity of KBB1–KBB6 samples: (a) hydroxyl radical species trapped by DMPO, (b) superoxide radical species trapped by DMPO/DMSO, (c) singlet oxygen species trapped by TEMP.

above observations, hydroxyl radicals ( $\cdot\text{OH}$ ), superoxide radicals ( $\cdot\text{O}_2^-$ ) and singlet oxygen ( $^1\text{O}_2$ ) were confirmed to be the main active species.

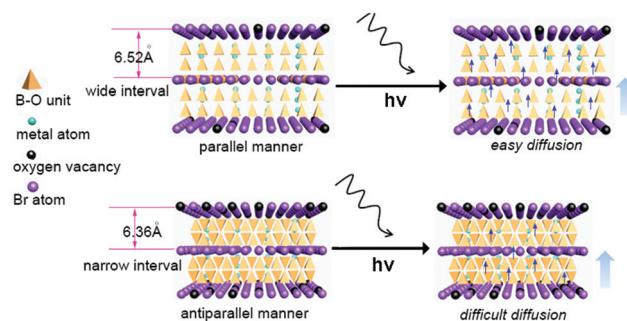
To determine the contributions of various reactive species in the dechlorination of the 2,4-DCP over the six KBB catalysts under the above reaction conditions, trapping experiments were performed by the addition of different radical-scavengers into the photoactivity system. The photogenerated reactive species were tested by using  $\text{AgNO}_3$ , *t*-BuOH, KI and benzoquinone (BQ) as a scavenger of electrons ( $e^-$ ),  $\cdot\text{OH}$ , VB hole ( $h^+$ ), and  $\cdot\text{O}_2^-$ , respectively. As illustrated in Fig. 11c, the degradation process slightly decreased with the addition of  $\text{AgNO}_3$ , which indicated that  $e^-$  had a weak effect on the photocatalytic degradation of 2,4-DCP. The photodegradation activity decreased somewhat after the addition of *t*-BuOH and KI, implying that  $\cdot\text{OH}$  and ( $h^+$ ) may participate in the photodegradation process. However, the photocatalytic performance was significantly suppressed by the addition of BQ, indicating that the photodegradation of 2,4-DCP predominantly proceeded *via*  $\cdot\text{O}_2^-$ . These observations indicate that the photoreaction process in this system is mainly dominated by  $\cdot\text{O}_2^-$ , and the  $\cdot\text{OH}$  and  $h^+$  played secondary roles.

Why is the activity of the polar materials superior to non-polar materials? In addition, why is an increase in Na content accompanied by the increase in the photoactivity in the non-polar materials? The plausible reasons are considered as follows:

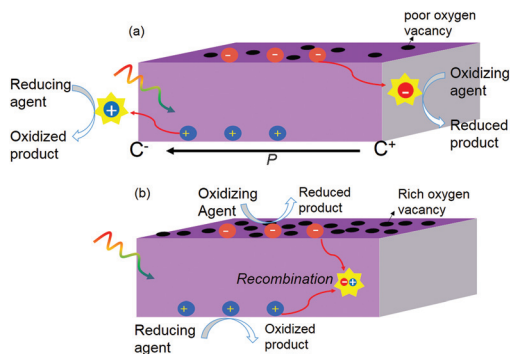
The first reason lies in the structural difference. From the different view directions, KBB1–KBB3 samples have a three dimensional structure with K and Br atoms loosely distributed in the large tunnel; this wide distance of the layers causes the  $[\text{B}_6\text{O}_{10}]$  units to align in parallel. When the light irradiation hits the surface, the wide interval allows the electrons to easily diffuse; we believe that this linkage is very helpful in forming charge delivery channels and the separation of photogenerated electron–hole pairs to obtain a very high photocatalytic activity. However, for the KBB4–KBB6 samples, the lattice becomes smaller with all the atoms packed

tightly,<sup>45</sup> which impairs the mobility of the charges and makes diffusion difficult.<sup>46</sup> When the surface is under irradiation, the charges are easily trapped and therefore, it is not favourable for the electron transfer. This suggests that for the different phases of KBB1–KBB6, the movement of electrons might occur more easily in a polar structure than in a nonpolar structure (Scheme 1).

The second reason is that the charge transfer motivation is different for the two phases. The higher charge injection efficiency for the KBB1–KBB3 samples, originating from the inherent internal static electric fields, is considered to be the main driving force for promoting the photocatalytic activity. The polarization field attracts the holes in the KBB1–KBB3 samples to shift toward the  $\text{C}^-$  side of the cube, while the electrons are repelled to the  $\text{C}^+$  side of the cube of the sample. This confirms that the built-in electric field can mitigate the photocatalytic process. The higher activity of KBB3 is simply because this catalyst has a higher Na content in the polar phase, which leads to a higher concentration of oxygen defects and makes a more active site to facilitate the charge separation (Scheme 2a). In nonpolar materials, the energy required to



**Scheme 1** Schematic illustration of the substitute atom content of polar and nonpolar KBB, accounting for the role of bulk atom arrangement on the diffusion and concentration of oxygen vacancies.



**Scheme 2** Possible carrier transfer in bulk motivation materials and surface defects are controlled during the 2,4-DCP degradation process.

form an oxygen vacancy increases rapidly towards the surface, where the coordination environment is changed, which correlates directly with the change in the phase transition process. The increase in the oxygen vacancy with the increase in the substitute content indicates that the oxygen vacancies are the primary active sites for the photocatalytic process, significantly benefiting the interfacial charge separation in the nonpolar photocatalytic system (Scheme 2b).<sup>47</sup>

In the above deduction, we can see that, in particular, for KBB3 polar materials, the oxygen vacancies and the built-in electric field take synergistic action on the degradation process, allowing the KBB3 sample to have the best performance. For nonpolar materials, the main active species only come from the high concentration of oxygen vacancies, thus making the activity of KBB6 better than KBB4 and KBB5 samples but inferior to KBB1–KBB3 samples (Scheme 2b). It has also been stated that the efficiency of KBB1 was superior to KBB6, which is due to the fact that the bulk charge separation deficiencies, depending on the orientations of the internal electrostatic fields, are much larger compared to the surface defects induced by the oxygen vacancies during the 2,4-DCP degradation process.

## Experimental

### Sample preparation

$M_2CO_3$  ( $M = Na, K$ ) and  $MBr$  ( $M = Na, K$ ) were obtained from Shanghai Shanpu Chemical Co. Ltd, and  $H_3BO_3$  was provided by Tianjin Baishi Chemical Industry Co. Ltd. Other reagents from commercial sources were used directly without further purification. A series of alkali metal bromide-borates,  $K_{3-x}Na_xB_6O_{10}Br$  with  $x = 0, 0.13, 0.67, 1.30, 2.20, 3$ , denoted as KBB1–KBB6 were prepared as reported previously.<sup>48</sup> The raw materials with a stoichiometric mixture of  $M_2CO_3$  ( $M = Na, K$ ),  $MBr$  ( $M = Na, K$ ), and  $H_3BO_3$  were well mixed, ground and then packed into a crucible and calcined to 450 °C for 4 h to release the  $CO_2$  and water, then maintained for 12 h at 710–715 °C for (KBB1, KBB2, KBB3), and 720–730 °C for (KBB4, KBB5, KBB6), respectively.

## Characterization

We used various techniques to test the as-prepared samples. The phase structures of the studied samples were characterized by X-ray diffraction (XRD) via a Bruker D8 Advance X-ray diffractometer. The diffuse reflectance absorption spectra (DRS) were obtained in the range from 200 to 800 nm using a Solidspec-3700 DUV spectrometer with  $BaSO_4$  as the reference. The morphologies of KBB samples were observed on a scanning electron microscope (SEM) using a ZEISS SUPRA55VP apparatus and the energy dispersive X-ray spectra (EDX) were obtained using the EDX8000. The Brunauer–Emmett–Teller (BET) surface area was determined from the  $N_2$  adsorption/desorption isotherms recorded at 77 K (QUADRASORB IQ, Quantachrome Instrument Corp.). Raman spectra were recorded by a HORIBA Jobin Yvon LabRAM HR confocal spectrometer at an excitation wavelength of 532 nm. The intermediate products during 2,4-DCP degradation were qualitatively analyzed by a liquid chromatography-mass spectrometry system (LC-MS, Agilent 1290) with a C18 column (4.6 mm × 250 mm). A mixture of methanol and water [80/20 (v/v)] was used as the effluent with a flow rate  $1 mL min^{-1}$ , and detector wavelength of 282 nm. Atomic force microscopy (AFM) combined with Kelvin probe force microscopy (KPFM) was conducted under ambient conditions with a Bruker Multimode 8. Fluorescence spectra were obtained on a Hitachi fluorescence spectrophotometer F-7000. Oxygen vacancies and  $^{\bullet}O_2^-$ ,  $^{\bullet}OH$ , and  $^1O_2$  reactive oxygen species were detected by the ESR technique at ambient temperature (Bruker E500, Germany). A NETZSCH STA 449C thermal analyser was used to analyse the thermal behaviour.

### Second harmonic generation (SHG) tests

For the powder SHG measurements, about 200 mg of powder was pressed into a pellet, which was then irradiated with a pulsed infrared beam (10 ns, 10 kHz) produced by a Q-switched Nd: YAG laser of wavelength 1064 nm. The double-frequency emission at 532 nm was recorded by an Apple 6s mobile phone.

## Conclusions

Six  $K_{3-x}Na_xB_6O_{10}Br$  materials were fabricated by a traditional solid-state reaction method. The phase structure, microstructure, photo dechlorinating properties and the reactive oxygen species were discussed. Different arrangements of  $[B_6O_{10}]$  groups and the coordination environments of metal atoms jointly contributed to the different crystal structures. The built-in electric field of the polar material was measured by the KPFM method. By tuning the substituted atom content, the concentration of surface oxygen vacancies can be controlled effectively. The photocatalytic activity also showed good correlation with the concentration of oxygen vacancies and the built-in electric field. We clearly proposed and confirmed that the built-in electric field and oxygen vacancies have a synergistic effect on the degradation of the 2,4-DCP, but the bulk

charge separation could play a more important role in determining the overall charge separation compared with the surface defects. In further investigations, the ratio of the surface oxygen vacancy and the built-in electric field will be clearly studied.

## Conflicts of interest

There are no conflicts to declare.

## Acknowledgements

This work was supported by the National Natural Science Foundation of China (51772325), and Natural Science Foundation of Xinjiang Uygur Autonomous Region (2016D01A072).

## Notes and references

- X. Chen, S. Shen, L. Guo and S. S. Mao, *Chem. Rev.*, 2010, **110**, 6503–6570.
- X. Wang and C. Li, *J. Photochem. Photobiol., C*, 2017, **33**, 165–179.
- U. G. Akpan and B. H. Hameed, *J. Hazard. Mater.*, 2009, **170**, 520–529.
- Y. Bi, S. Ouyang, N. Umezawa, J. Cao and J. Ye, *J. Am. Chem. Soc.*, 2011, **133**, 6490–6492.
- S. Luo, M. Tang, P. K. Shen and S. Ye, *Adv. Mater.*, 2017, **29**, 1601687–1601692.
- H. Huang, Y. He, X. Li, M. Li, C. Zeng, F. Dong, X. Du, T. Zhang and Y. Zhang, *J. Mater. Chem. A*, 2015, **3**, 24547–24556.
- J. Low, J. Yu, M. Jaroniec, S. Wageh and A. Al-Ghamdi Ahmed, *Adv. Mater.*, 2017, **29**, 1601694.
- H. Wang, L. Zhang, Z. Chen, J. Hu, S. Li, Z. Wang, J. Liu and X. Wang, *Chem. Soc. Rev.*, 2014, **43**, 5234–5244.
- D. Jiang, W. Wang, L. Zhang, Y. Zheng and Z. Wang, *ACS Catal.*, 2015, **5**, 4851–4858.
- M. Nolan, A. Iwaszuk, A. K. Lucid, J. J. Carey and M. Fronzi, *Adv. Mater.*, 2016, **28**, 5425–5446.
- Z. Zou, J. Ye, K. Oka and Y. Nishihara, *Phys. Rev. Lett.*, 1998, **80**, 1074–1077.
- D. A. Muller, N. Nakagawa, A. Ohtomo, J. L. Grazul and H. Y. Hwang, *Nature*, 2004, **430**, 657.
- H. Li, J. Shang, Z. Yang, W. Shen, Z. Ai and L. Zhang, *Environ. Sci. Technol.*, 2017, **51**, 5685–5694.
- B. Wang, X. Wang, L. Lu, C. Zhou, Z. Xin, J. Wang, X.-k. Ke, G. Sheng, S. Yan and Z. Zou, *ACS Catal.*, 2018, **8**, 516–525.
- N. Tayebi, S. Kim, R. J. Chen, Q. Tran, N. Franklin, Y. Nishi, Q. Ma and V. Rao, *Nano Lett.*, 2012, **12**, 5455–5463.
- L. Li, P. A. Salvador and G. S. Rohrer, *Nanoscale*, 2014, **6**, 24–42.
- H. Huang, S. Tu, C. Zeng, T. Zhang, H. Reshak Ali and Y. Zhang, *Angew. Chem., Int. Ed.*, 2017, **56**, 11860–11864.
- H. Li, J. Li, Z. Ai, F. Jia and L. Zhang, *Angew. Chem., Int. Ed.*, 2018, **57**, 122–138.
- M. Li, Y. Dai, X. Ma, T. Jing and B. Huang, *Appl. Catal., B*, 2017, **205**, 211–218.
- X. Fan, L. Zang, M. Zhang, H. Qiu, Z. Wang, J. Yin, H. Jia, S. Pan and C. Wang, *Chem. Mater.*, 2014, **26**, 3169–3174.
- O. F. Lopes, K. T. G. Carvalho, A. E. Nogueira, W. Avansi and C. Ribeiro, *Appl. Catal., B*, 2016, **188**, 87–97.
- M. H. Park, T. Schenk, M. Hoffmann, S. Knebel, J. Gärtner, T. Mikolajick and U. Schroeder, *Nano Energy*, 2017, **36**, 381–389.
- Z. Zou, J. Ye and H. Arakawa, *J. Mol. Catal. A: Chem.*, 2001, **168**, 289–297.
- R. T. Sanderson, *J. Inorg. Nucl. Chem.*, 1966, **28**, 1553–1565.
- D. C. Ghosh and T. Chakraborty, *J. Inorg. Nucl. Chem.*, 2009, **906**, 87–93.
- X. Fan, S. Pan, X. Hou, X. Tian, J. Han, J. Haag and K. R. Poeppelmeier, *Cryst. Growth Des.*, 2010, **10**, 252–256.
- Q. Huang, M. Ulutagay, P. A. Michener and S.-J. Hwu, *J. Am. Chem. Soc.*, 1999, **121**, 10323–10326.
- H. Wang and G. Wu, *J. Phys. Chem. Solids*, 1999, **60**, 129–137.
- M. He, X. Chen, H. Okudera and A. Simon, *Chem. Mater.*, 2005, **17**, 2193–2196.
- M. M. Shvebelman, A. G. Agronin, R. P. Urenski, Y. Rosenwaks and G. I. Rosenman, *Nano Lett.*, 2002, **2**, 455–458.
- S. Ida, A. Takashiba, S. Koga, H. Hagiwara and T. Ishihara, *J. Am. Chem. Soc.*, 2014, **136**, 1872–1878.
- Z. Lou, M. Zhu, X. Yang, Y. Zhang, M.-H. Whangbo, B. Li and B. Huang, *Appl. Catal., B*, 2018, **226**, 10–15.
- T. Soltani and B.-K. Lee, *J. Hazard. Mater.*, 2016, **316**, 122–133.
- S. Yan, J. Wang, H. Gao, N. Wang, H. Yu, Z. Li, Y. Zhou and Z. Zou, *Adv. Funct. Mater.*, 2013, **23**, 758–763.
- M. V. Ganduglia-Pirovano, A. Hofmann and J. Sauer, *Surf. Sci. Rep.*, 2007, **62**, 219–270.
- P. Yu, K. Zhang, H. Huang, M. Wen, Q. Li, W. Zhang, C. Hu and W. Zheng, *Appl. Surf. Sci.*, 2017, **410**, 470–478.
- J. Li, M. Zhang, Z. Guan, Q. Li, C. He and J. Yang, *Appl. Catal., B*, 2017, **206**, 300–307.
- L. Hou, M. Zhang, Z. Guan, Q. Li and J. Yang, *Appl. Surf. Sci.*, 2018, **428**, 640–647.
- G. Pacchioni, *ChemPhysChem*, 2003, **4**, 1041–1047.
- Z. Lou, P. Wang, B. Huang, Y. Dai, X. Qin, X. Zhang, Z. Wang and Y. Liu, *ChemPhotoChem*, 2017, **1**, 136–147.
- S. Wang, X. Ding, X. Zhang, H. Pang, X. Hai, G. Zhan, W. Zhou, H. Song, L. Zhang, H. Chen and J. Ye, *Adv. Funct. Mater.*, 2017, **27**, 1703923.
- W. Shi, F. Guo and S. Yuan, *Appl. Catal., B*, 2017, **209**, 720–728.
- J. Di, J. Xia, H. Li, S. Guo and S. Dai, *Nano Energy*, 2017, **41**, 172–192.
- S. Lan, J. Feng, Y. Xiong, S. Tian, S. Liu and L. Kong, *Environ. Sci. Technol.*, 2017, **51**, 6560–6569.

- 45 S. J. Han, Y. Wang, S. L. Pan, X. Y. Dong, H. P. Wu, J. Han, Y. Yang, H. W. Yu and C. Y. Bai, *Cryst. Growth Des.*, 2014, **14**, 1794–1801.
- 46 Z. Zou, J. Ye, R. Abe and H. Arakawa, *Catal. Lett.*, 2000, **68**, 235–239.
- 47 H.-S. Kim, J. B. Cook, H. Lin, J. S. Ko, S. H. Tolbert, V. Ozolins and B. Dunn, *Nat. Mater.*, 2016, **16**, 454.
- 48 P. A. Plachinda, V. A. Dolgikh, S. Y. Stefanovich and P. S. Berdonosov, *Solid State Sci.*, 2005, **7**, 1194–1200.